"GLOBAL MAGNETOHYDRODYNAMIC MODELING OF THE SOLAR CORONA"

FINAL REPORT

(2/07/95—2/06/98)

Science Applications International Corporation

An Employee-Owned Company

NASA CONTRACT: NASW-4968

SPACE PHYSICS SUPPORTING RESEARCH AND TECHNOLOGY (SR&T),

AND SUBORBITAL PROGRAM

PRINCIPAL INVESTIGATOR:

JON A. LINKER

SCIENCE APPLICATIONS INTERNATIONAL CORPORATION

10260 CAMPUS POINT DRIVE

SAN DIEGO, CA 92121-1578

Global Magnetohydrodynamic Modeling of the Solar Corona

NASA Contract NASW-4968 (2/07/95-2/06/98)

P.I.: Jon Linker

Final Report

1. Introduction

The coronal magnetic field defines the structure of the solar corona, the position of the heliospheric current sheet, the regions of fast and slow solar wind, and the most likely sites of coronal mass ejections. There are few measurements of the magnetic fields in the corona, but the line-of-sight component of the global magnetic fields in the photosphere have been routinely measured for many years (for example, at Stanford's Wilcox Solar Observatory, and at the National Solar Observatory at Kitt Peak). The SOI/MDI instrument is now providing high-resolution full-disk magnetograms several times a day. Understanding the large-scale structure of the solar corona and inner heliosphere requires accurately mapping the measured photospheric magnetic field into the corona and outward.

Ideally, a model should not only extrapolate the magnetic field, but should self-consistently reconstruct both the plasma and magnetic fields in the corona and solar wind. Support from our NASA SR&T contract has allowed us to develop three-dimensional magnetohydrodynamic (MHD) computations of the solar corona that incorporate observed photospheric magnetic fields into the boundary conditions. These calculations not only describe the magnetic field in the corona and interplanetary space, but also predict the plasma properties as well. Our computations thus far have been successful in reproducing many aspects of both coronal and interplanetary data, including the structure of the streamer belt, the location of coronal hole boundaries, and the position and shape of the heliospheric current sheet.

The most widely used technique for extrapolating the photospheric magnetic field into the corona and heliosphere are potential field models, such as the potential field source-surface model (PFSS) (*Schatten et al.*, 1969; *Altschuler and Newkirk*, 1969; *Hoeksema*, 1984, 1991) and the potential field current-sheet (PFCS) model

(*Schatten*, 1971).

The potential field models have been shown to describe many aspects of coronal and interplanetary data (e.g., *Wang and Sheeley*, 1988; *Hoeksema and Suess*, 1990; *Wang and Sheeley*, 1992), and the models are still being improved (*Schulz*, 1995; *Zhao and Hoeksema*, 1995). Ease of computation makes these models especially useful tools, but the simplifying assumptions underlying these methods limit their applicablility. The coronal phenomena of interest are large-scale and long-wavelength, and are thus well described by the magnetohydrodynamic (MHD) equations. Magnetostatic solutions (*Bogdan and Low*, 1986; *Bagenal and Gibson*, 1991; *Gibson and Bagenal*, 1995; *Gibson et al.*, 1996) can describe the density distribution in the lower corona but cannot model the solar wind. Full MHD computations (including flow terms) contain much of the physics required for describing the solar corona and inner heliosphere. At the inception of our NASA-supported project, MHD computations of helmet streamers had been performed for many years (e.g., *Endler*, 1971; *Pneuman and Kopp*, 1971; *Steinolfson et al.*, 1982; *Washimi et al.*, 1987; *Linker et al.*, 1990; *Wang et al.*, 1993; *Linker and Mikić*, 1995; *Stewart and Bravo*, 1996). However, these calculations typically used idealized magnetic flux distributions (such as a dipole or other multipole component), and most were limited to two dimensions. The resulting configurations could only be compared to the corona in terms of abstract qualities, and not specific observations.

To perform a realistic 3-D MHD computation of the corona, it is necessary to incorporate realistic magnetic fields into the boundary conditions (*Mikić and Linker*, 1996; *Linker et al.*, 1996; *Usmanov*, 1996). We have developed numerical MHD computations of the corona and inner heliosphere that incorporate observed photospheric magnetic fields. In Section 2, we briefly describe the methodology of our computations. Section 3 shows comparisons of our results with specific observations. Section 4 describes improvements to the model that are presently being investigated.

2. Modeling the Corona and Inner Heliosphere

To compute self-consistent three-dimensional MHD solutions for the large-scale

corona, we solve the following form of the equations in spherical coordinates (*Mikić and Linker*, 1994, describes the method):

$$\nabla \times \mathbf{B} = \frac{4\pi}{c}\mathbf{J} \tag{1}$$

$$\frac{1}{c}\frac{\partial \mathbf{B}}{\partial t} = -\nabla \times \mathbf{E} \tag{2}$$

$$\mathbf{E} + \frac{\mathbf{v} \times \mathbf{B}}{c} = \eta \mathbf{J} \tag{3}$$

$$\frac{\partial \rho}{\partial t} + \nabla \cdot (\rho \mathbf{v}) = 0 \tag{4}$$

$$\rho \left(\frac{\partial \mathbf{v}}{\partial t} + \mathbf{v} \cdot \nabla \mathbf{v} \right) = \frac{1}{c}\mathbf{J} \times \mathbf{B} - \nabla p - \nabla p_w + \rho \mathbf{g} + \nabla \cdot (\nu \rho \nabla \mathbf{v}) \tag{5}$$

$$\frac{\partial p}{\partial t} + \nabla \cdot (p\mathbf{v}) = (\gamma - 1)(-p \nabla \cdot \mathbf{v} + S) \tag{6}$$

where $\mathbf{B}$ is the magnetic field intensity, $\mathbf{J}$ is the electric current density, $\mathbf{E}$ is the electric field, $\mathbf{v}$, ρ, and p are the plasma velocity, mass density, and pressure. The gravitational acceleration is $\mathbf{g}$, γ is the ratio of specific heats, η is the resistivity, ν is the viscosity, S represents energy source terms, and the wave pressure p_w represents the acceleration due to Alfvén waves [*Jacques*, 1977; *Hollweg*, 1978].

The term S in equation (6) includes the effects of coronal heating, thermal conduction parallel to $\mathbf{B}$, radiative losses, and Alfvén wave dissipation (viscous and resistive dissipation can also be included). S and P_w were set to zero for the results discussed in this section, which restricts us to examining polytropic solutions (i.e., $dP\rho^{-\gamma}/dt = 0$). These solutions have the advantage that relatively simple models can match many of the properties of the corona; however, values of γ close to 1 ($\gamma = 1.05$ for the results shown here) are necessary to produce plasma profiles that are similar to coronal observations (*Parker*, 1963). This reflects the importance of the processes embodied in S that we have neglected here. Section 4 describes the incorporation of these processes.

The methods we use to solve equations (1-6), including the boundary conditions, have been described previously (*Mikić and Linker*, 1994, 1996; *Linker et al.* 1996; *Linker and Mikić*, 1997). We have used synoptic magnetograms from the Wilcox Solar Observatory at Stanford and the National Solar Observatory at Kitt

Peak (collected during a solar rotation by daily measurements of the line-of-sight magnetic field at central meridian) to specify the radial magnetic field (B_r) at the photosphere (in the manner described by *Wang and Sheeley*, 1992). We also specify the density and pressure at the lower boundary. For the initial condition, we compute the potential (current-free) field consistent with the specified distribution of B_r at the lower boundary, and a wind solution [*Parker*, 1963] consistent with the specified ρ and p. We then solve equations (1-6). The configuration evolves until a steady state is reached, when the magnetic field lines and plasma state have settled into equilibrium. A typical run of our code on a relatively coarse (nonuniform) computational mesh ($81 \times 51 \times 32$ r,θ,ϕ mesh points) takes about an hour of Cray-C90 CPU time per day of real time, while higher-resolution runs ($101 \times 101 \times 64$) take a few hours of CPU time per day of real time. Coronal computations relax to a steady state in a few days of real time.

3. Comparisons with Observations

The solutions obtained in the manner described in Section 2 can in principle provide a 3-D description of the corona and inner heliosphere, including the detailed distribution of magnetic fields, currents, plasma density, and temperature. The validity of this approach can only be verified through comparison with observations. With this goal in mind we have sought to compute solutions for specific time periods of interest. Carrington rotation 1892 (CR1892, January 27–February 23, 1995) is good example: a variety of coronal data is available for that time period (Mauna Loa white light images, Yohkoh soft X-ray images, and coronal hole boundaries based on the Kitt Peak 10830 images). At the same time Ulysses probed the heliosphere over a wide range of latitudes. We used a Kitt Peak synoptic map to specify B_r in the manner described in Section 2, and computed a solution out to 400 solar radii (1.9 astronomical units, or A.U.). Figure 1 shows how the solution captures coronal structures near the Sun and also models the inner heliospere.

Coronal or helmet streamers appear as bright regions in white-light coronal images; they are believed to outline closed magnetic regions on the Sun. To directly compare our results with observations, we must develop images like those obtained

Magnetohydrodynamic Modeling of the Solar Corona and Inner Heliosphere: Carrington Rotation 1892 (January 27 – February 23, 1995)

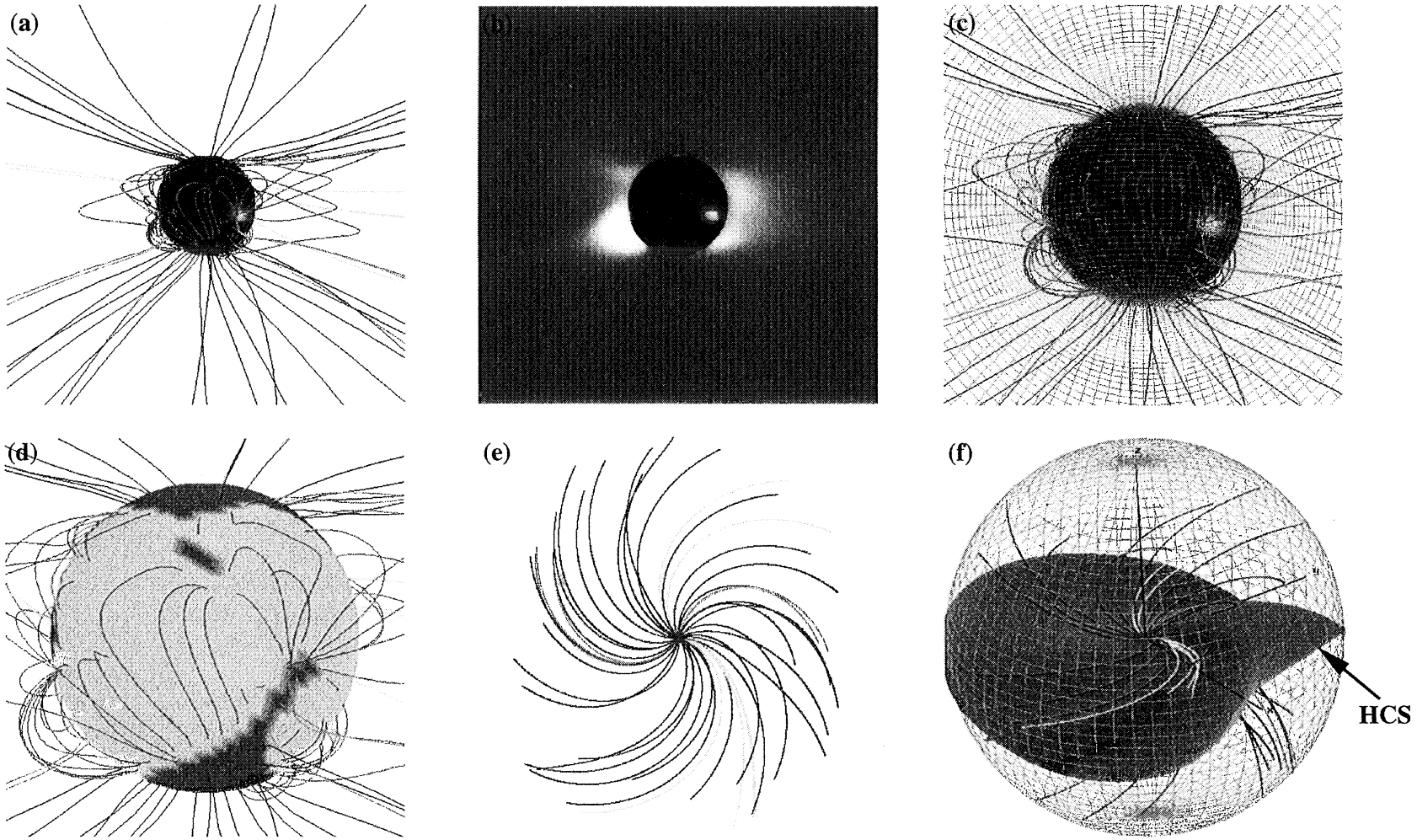

Figure 1. An MHD calculation of the solar corona and inner heliosphere for Carrington Rotation CR1892, showing (**a**) magnetic field lines (|B| is contoured on the solar surface) (**b**) the polarization brightness (pB) (**c**) mesh close to the Sun (**d**) boundary between open field regions (coronal holes, shown as dark gray) and closed field regions (light gray) (**e**) spiral field lines viewed from 1.9 A.U. above the pole of the Sun (**f**) mesh at 1.9 A.U., with an isosurface showing the position of the heliospheric current sheet. The variety of coronal and interplanetary properties predicted by the calculation allow the results to be tested against a wide range of data sets.

with coronagraphs and during eclipses. Frequently the polarization brightness (pB) is the observed quantity. The distribution of pB in the plane of the sky is proportional to the line-of-sight integral of the product of the electron density and a scattering function that varies along the line of sight (*Billings*, 1966). Using the plasma density from our computation, we can calculate pB and compare it with actual observations. Eclipse and coronagraph images typically compensate for the rapid fall off of coronal density, through the use of radially graded filters or the vignetting properties of the coronagraph. We detrend our computed pB in a similar manner. Figure 2 shows a comparison between the predicted pB from our computation with Mauna Loa Coronameter data. Throughout the rotation, the results from the MHD computation correspond well with the observations. This computation, along with those we have performed for other time periods, support the long-held belief that the magnetic field distribution on the Sun controls the position and shape of the streamer belt.

Open field regions on the Sun (coronal holes) are the source of the solar wind. Another way we can test the MHD model is to compare open field regions from the computation with coronal holes observed from solar images. By tracing field lines at each grid point and determining whether the field lines were open (reached the outer boundary) or closed (returned to the Sun), we mapped the open field regions predicted by our computation and compared them with Yohkoh soft X-ray images, as shown in Figure 3. Coronal holes typically show up as dark regions in X-rays. Throughout the rotation, the coronal hole boundaries predicted by the model agree reasonably well with the dark regions seen in Yohkoh, although there are also some discrepancies. It is important to note that the identification of coronal holes in soft X-ray images (or the Kitt Peak 10830 line) is somewhat subjective. In X-rays, neighboring coronal emission can obscure coronal holes, and the absence of emission can also occur in quiet closed field regions. As part of a coordinated study for the time period of the Ulysses fast latitude scan (*Neugebauer et al.*, 1997), the coronal hole boundaries from our model were also compared with the He 10830 observations from Kitt Peak. Reasonable correspondence was again found, although it is interesting to note that not only were there some disagreements between the

Comparison of a 3D MHD Model of CR1892 with Mauna Loa Coronameter Data (HAO)

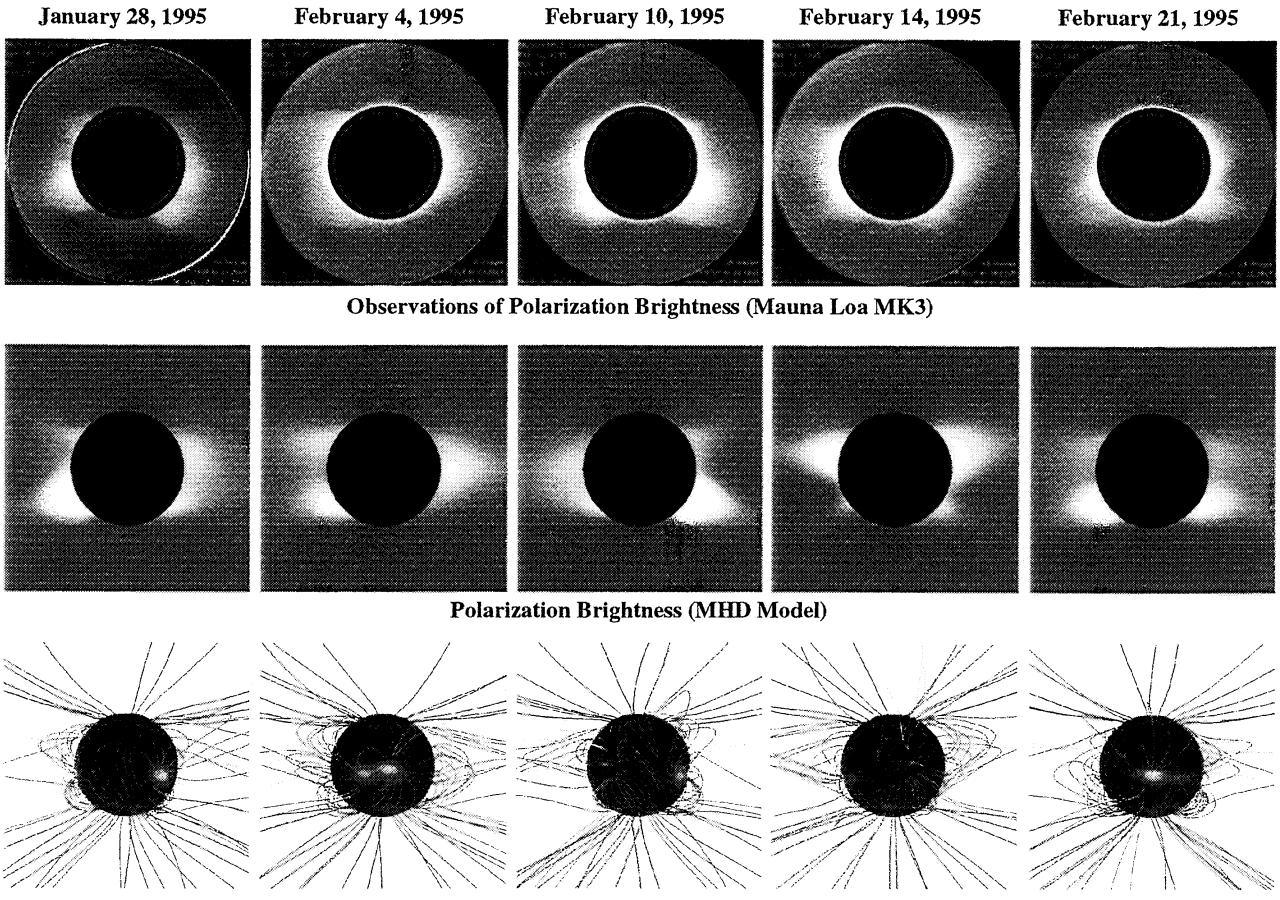

Figure 2. Comparison of Mauna Loa Coronameter data (top panels) with the polarization brightness (pb) computed from the MHD simulation (middle panels). The model results correspond well to the observations throughout the rotation. In the bottom set of panels traces of the magnetic field lines are shown, with the magnitude of the magnetic field contoured on the solar surface. The strongest fields (yellow colors) correspond to active regions.

Comparison of Coronal Hole Boundaries: A 3D MHD Model of CR1892 and Yohkoh Data

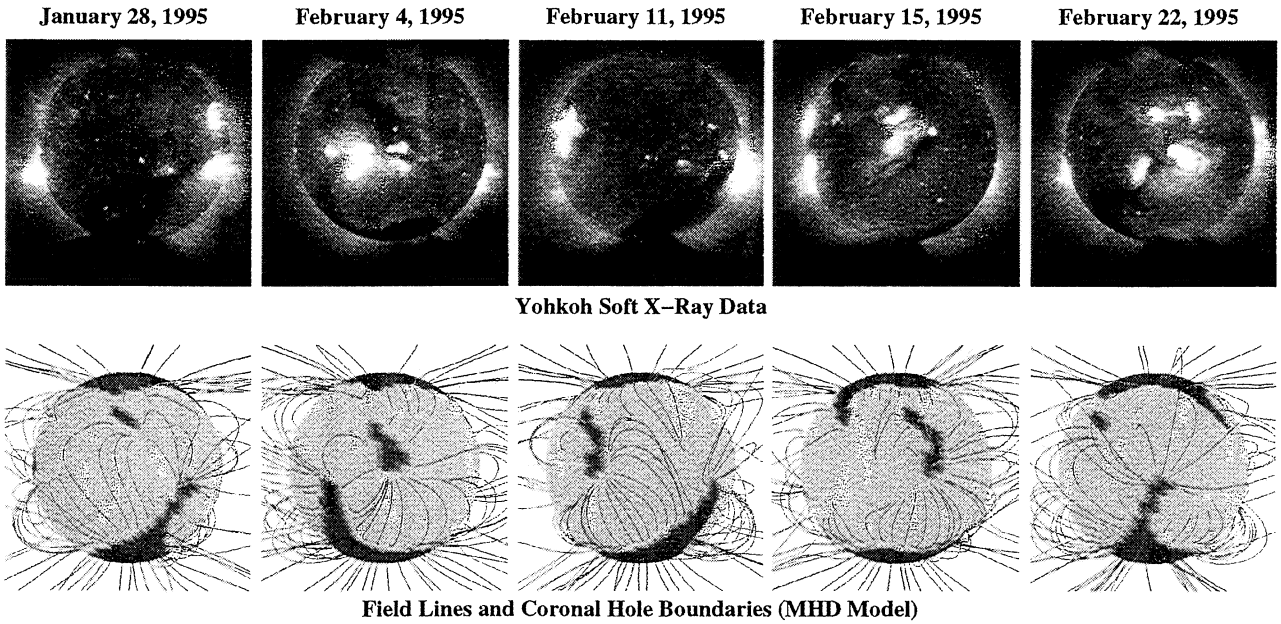

Figure 3. Comparison of Yohkoh soft X–ray images (top panels) with the open field regions predicted by the MHD simulation. Identification of coronal hole boundaries in Yohkoh data can be somewhat subjective. The darkest regions often correspond to coronal holes (although the absence of emission can occur in closed field regions, and coronal holes can be obscured by neighboring emission). Nevertheless, the coronal hole boundaries predicted by the MHD calculation (shown in dark gray) correspond approximately to those seen in the Yohkoh data.

coronal holes predicted by the model and the absence of emission in the observations, coronal hole boundaries in He 10830 and the dark regions in Yohkoh also did not always correspond.

The comparisons of our results with coronal data shows that the basic large-scale structure of the corona has been captured in the model. We have also compared our results with interplanetary data. During February–April, 1995 (Carrington rotations 1892–1894), the Ulysses spacecraft sampled a wide range of heliographic latitude in a relatively short period of time; this time period has since been referred to as the fast latitude scan. Figure 4 (red curve) shows "simulated" Ulysses data, created by flying the Ulysses trajectory through the MHD solution and extracting B_r along the trajectory. For comparison, the actual B_r measured by Ulysses is also shown (blue curve). The fluctuations in the solar wind data are caused by turbulent waves and transient phenomena, and thus are not present in the MHD model, but the model does reproduce the correct magnitude and polarity of the field, including many of the heliospheric current sheet crossings. Not surprisingly, the model matches the data best during and shortly after CR1892, when the photospheric data used to perform the calculation is most applicable. Photospheric data for the subsequent rotations shows that the magnetic field is indeed evolving.

Figure 5 shows the heliospheric current sheet predicted by our computation for CR1892, depicted as an isosurface. The Ulysses trajectory in the rotating frame of the Sun is shown. Blue colors for the trajectory correspond to times when negative B_r fields were observed, and red colors show times when positive B_r fields were observed. The dominant polarity observed by Ulysses agrees with that predicted by the simulation for most of the early (lower) part of the trajectory. In the later part of the trajectory, there is a passage into negative polarity not predicted by the model (this can also be seen in Figure 4 around day-of-year 85). As this occurred in CR1894, it is possible that the heliospheric magnetic field has changed significantly from CR1892 (two months earlier). To test this possibility, we computed MHD models for rotations CR1893 and CR1894 as well. Figure 6 shows a comparison of heliospheric current sheet (HCS) crossings observed by Ulysses and projected back to the Sun (*Smith et al.* 1995) with the HCS predicted by the MHD model for

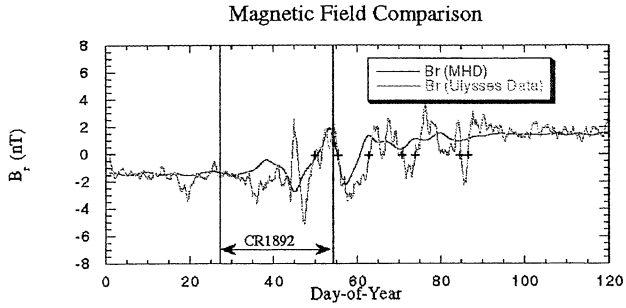

Figure 4. A comparison of a simulated time series of B_r for the MHD computation of CR1892 (red curve) with Ulysses data (blue curve). Heliospheric current sheet crossings identified by *Smith et al.* (1995) are marked as crosses (transient phenomena can also cause B_r to change sign). The time period for CR1892 (when the photospheric data used by the MHD calculation is most applicable) is marked on the plot. The MHD calculation reproduces the correct magnitude of the field and matches many of the current sheet crossings. Not surprisingly, the MHD results match the data best during or close to the CR1892 time period.

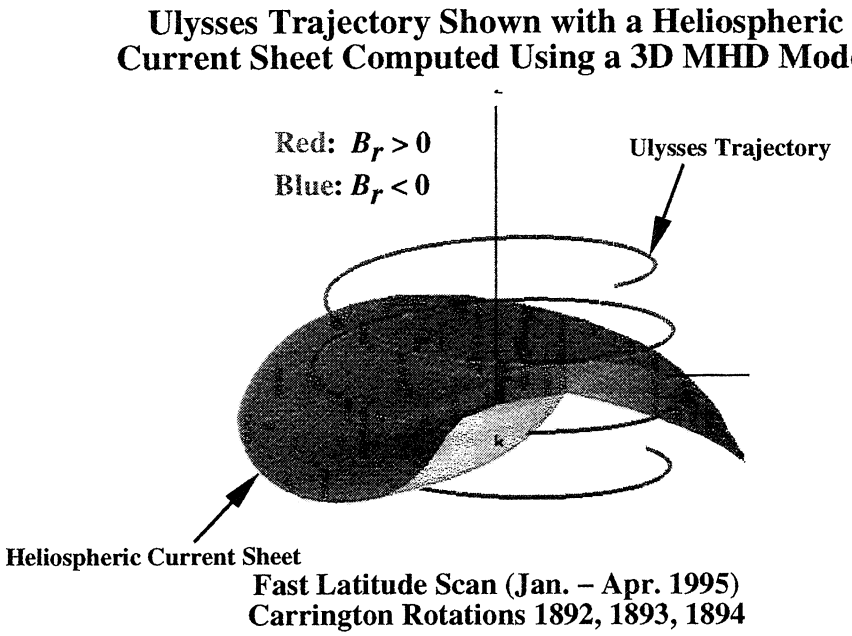

Figure 5. The heliospheric current sheet (HCS) predicted by the MHD computation of CR1892 shown in Figure 1. The Ulysses trajectory (red and blue curve) is shown in the rotating frame of the Sun. The colors of the trajectory indicate the polarity of the magnetic field observed by Ulysses. Fluctuations in B_r are present because of waves and transients in the solar wind, but the dominant polarity observed by Ulysses is similar to that predicted by the MHD computation.

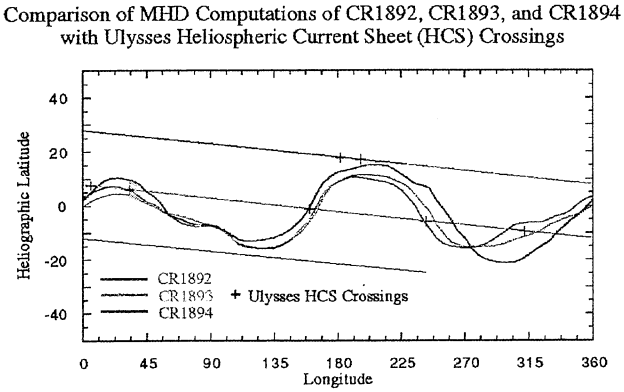

Figure 6. The HCS predicted by MHD computations of CR1892, CR1893, and CR1894 (red, blue, and green curves) and the Ulysses trajectory during this time (red, blue, and green lines) projected back at the Sun. HCS crossings from Ulysses identified by *Smith et al.* (1995) (also projected back to the Sun) are shown as crosses. There is overall good agreement between the predicted HCS crossings (where the Ulysses trajectory intersects the computed HCS) and the observed crossings. The MHD calculations predict that the HCS moved higher in latitude in the north during CR1894, as seen in the data. However, the uppermost crossings observed by Ulysses are not predicted by the model. Sensitivity of the calculations to the polar fields (poorly determined by line–of–sight magnetograms) could be a possible reason for this difference.

the two rotations. The red, blue and green straight lines show the Ulysses trajectory for CR1892, CR1893, and CR1894, respectively, and the red, blue, and green curves show the predicted HCS for these rotations. There is overall good agreement between the predicted HCS crossings (where the Ulysses trajectory intersects the model HCS) and the observed crossings (marked as +). The MHD calculations based on the photospheric data for CR1893 and CR1894 predict that the heliospheric magnetic field should have evolved during this time period and that the HCS should have moved to higher northern latitudes for CR1894, consistent with the observations. However, the two uppermost crossings are still not predicted by the model. We note that the tilt of the HCS (and thus its extent in northern and southern latitudes) can be strongly influenced by the polar fields, which are not well determined by line-of-sight magnetograms.

We have also computed MHD solutions for a number of other time periods of interest, including the last three total solar eclipses (see Figure 7). These and other comparisons of our MHD solutions with observations show that the MHD model typically does a good job of reproducing many aspects of coronal structure. While the success of the model has been encouraging, there is still significant room for improvement. In the next section, we describe how we are working refine and extend the physics in our computations to provide a tool capable of addressing important aspects of coronal structure that are beyond the scope of the present model.

4. An Improved Model of the Corona and Solar Wind

Starting at the photosphere and rising upward into the solar atmosphere, the temperature rises steeply in the chromosphere and transition region. The detailed coronal heating mechanism is not yet understood (see *Parker*, 1994 for a recent review), but most coronal heating mechanisms imply that this sharp temperature rise is the result of a volumetric heat source in the corona. In the inner corona, the large parallel thermal conductivity tends to make the temperature relatively uniform (on the order of $1\text{–}2\times10^6$ °K). The density at the top of the transition region is determined by the balance between radiation loss in the chromosphere and heating

ECLIPSE COMPARISONS

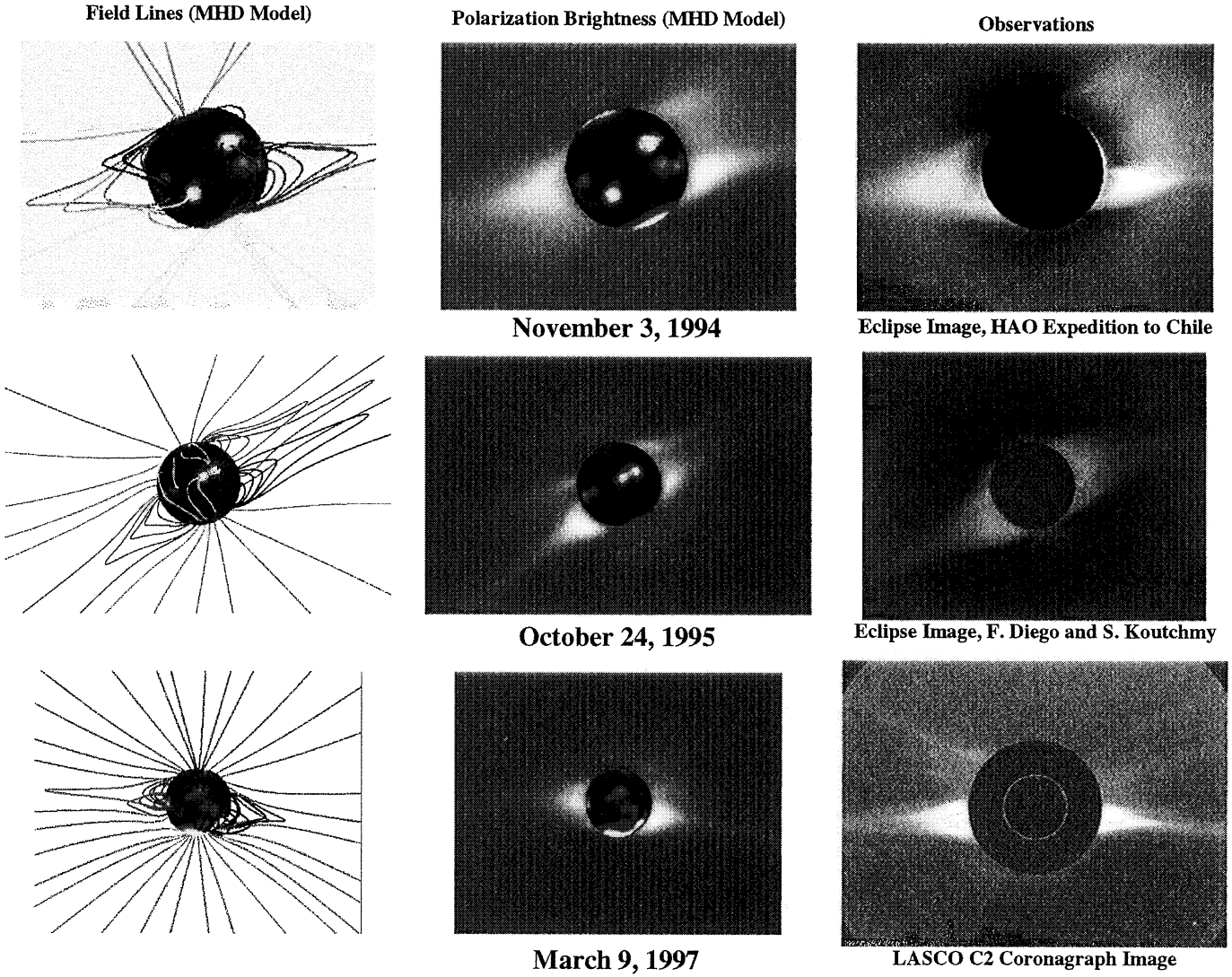

Figure 7. Comparison of MHD computations of the solar corona with eclipse observations. For the November 3, 1994 solar eclipse, we used a synoptic magnetogram for Carrington rotation 1888 (October 10 – November 6, 1994) as boundary conditions for the model, and we compared with the results subsequent to the eclipse. For the October 24, 1995 and March 9, 1997 solar eclipses, we used synoptic magnetograms from the rotation prior to the eclipse (CR1900: September 2 – September 29, 1995, and a combination of CR1918 and 1919: January 30 – February 26, 1997) to predict the structure in advance. All of these calculations used synoptic magnetograms from the Wilcox Solar Obsevatory. For the March 9 eclipse, no eclipse data is yet available. Comparison with an image from the LASCO coronagraph aboard the SOHO spacecraft is shown. These and other coronal modeling results can be found on our WEB page: http://iris023.saic.com:8000/corona/modeling.html

by thermal conduction from the hot corona (*Withbroe*, 1988). As we extend into the outer solar corona and interplanetary medium, the temperature decreases slowly as a result of solar wind acceleration and thermal conduction losses. Beyond about 10 R_s (where R_s is the solar radius), the plasma becomes collisionless, reducing the thermal conduction (*Hollweg*, 1978). In this region, solar wind acceleration by Alfvén waves can be important, and may be necessary to produce the observed fast solar wind at 1 A.U.

For the solutions described in Section 2, the use of a polytropic energy equation with a reduced polytropic index γ is an attempt to combine all these effects into a simplified energy equation. However, not surprisingly, this simple model fails to reproduce the fast ($\approx$ 800 km/s) and slow ($\approx$ 400 km/s) wind streams that are measured in interplanetary space. The nearly uniform coronal temperature that results from this model implies that the density scale height does not change much between the open and closed field regions, and so the magnitude of the density contrast between coronal holes and streamers is also not reproduced.

It is the complicated interplay of radiation loss, thermal conduction, coronal heating, and Alfvén wave acceleration and dissipation that describes the acceleration of the solar wind from the inner solar corona into the heliosphere. Fortunately, we can benefit from the considerable amount of research that has already been performed with one-dimensional MHD and multi-fluid models (*Withbroe*, 1988; *Habbal et al.*, 1995). These models have been quite successful, despite their obvious geometrical limitations, in modeling thermodynamic processes in the solar wind and in comparisons with spacecraft solar wind measurements (*Esser and Habbal*, 1995; *Habbal et al.*, 1996). The prescription for improving our coronal model follows naturally from existing 1-D models, and requires the inclusion of the effects described above in the energy and momentum equations of the 3-D MHD model. Some of these effects (heating and thermal conduction) have previously been included in 2-D MHD models (*Suess et al.*, 1996). The advantage of a multi-dimensional MHD calculation is that the magnetic field geometry (i.e., the location and distribution of open and closed field regions) is determined self-consistently, eliminating the parameters in the 1-D models that specify the flux tube geometry (the so-called

"expansion factor"). As has been done in 1-D models, the inner boundary is now chosen to be within the transition region, at a temperature of $T_0 = 500,000°\mathrm{K}$. The balance of radiation loss and thermal conduction within the chromosphere and transition region determines the density at the inner boundary from the condition (*Withbroe*, 1988)

$$C n_e^2 T_0^2 \int_{T_{ch}}^{T_0} Q(T) T^{1/2}\, dT = \frac{1}{2} q_0^2(T_0) \tag{7}$$

where n_e is the electron density at the inner boundary, C is a known constant, $q_0(T_0)$ is the thermal conduction heat flux at T_0, and the integral is performed from the base of the chromosphere (at $T_{ch} \approx 6000°\mathrm{K}$) through the top of the transition region (at $T = T_0$). The boundary conditions on the velocity are determined from the characteristic equations (*Linker and Mikić*, 1995, 1997; *Mikić and Linker*, 1996). Therefore, in this formulation, the only boundary conditions required from observations at the lower boundary $r = R_s$ are on the radial magnetic field.

The energy equation (6) becomes

$$\frac{\partial p}{\partial t} + \nabla \cdot (p\mathbf{v}) = (\gamma - 1)(-p \nabla \cdot \mathbf{v} - \nabla \cdot \mathbf{q} - n_e n_p Q(T) + H_{ch} + D) \tag{8}$$

where $\mathbf{q} = -\kappa_{\|} \hat{\mathbf{b}}\hat{\mathbf{b}} \cdot \nabla T$ is the parallel (along $\mathbf{B}$) thermal conduction heat flux, H_{ch} is the coronal heating source, D is the Alfvén wave dissipation term, n_e and n_p are the electron and proton density, and $Q(T)$ is the radiation loss function (*Rosner et al.*, 1978). The parallel thermal conductivity $\kappa_{\|}$ is the Spitzer value in the collisional regime, $\kappa_{\|} = 9 \times 10^7 T^{5/2}$ [erg/cm^2/s], with T in degrees K, and is reduced in the collisionless regime (beyond $\approx 10 R_s$); the representation in this regime is parameterized as a collisionless heat flux (*Hollweg*, 1978).

Results from previous 1-D computations suggest that an additional source of energy and momentum is necessary to accelerate the solar wind. Alfvén waves of solar origin are considered to be the most likely candidate (*Hollweg*, 1978; *Withbroe*, 1988). The acceleration of the solar wind by Alfvén waves occurs on a spatial and time scale that is below the spatial and time resolution of a global numerical model. In 1-D models, this effect is included using an equation for the time-space averaged Alfvén wave energy density ϵ (*Jacques*, 1977)

$$\frac{\partial \epsilon}{\partial t} + \nabla \cdot \mathbf{F} = \mathbf{v} \cdot \nabla p_w - D \tag{9}$$

where $\mathbf{F} = (\frac{3}{2}\mathbf{v} + \mathbf{v_A})\epsilon$ is the Alfvén wave energy flux, $v_A = B/\sqrt{4\pi\rho}$ is the Alfvén speed, $\mathbf{v_A} = \pm\hat{\mathbf{b}}v_A$ is the Alfvén velocity, and $p_w = \frac{1}{2}\epsilon$ is the Alfvén wave pressure that appears in the momentum equation (5) and represents the force on the plasma by Alfvén waves. To incorporate equation (9) in a multi-dimensional implementation, it is necessary to transport two Alfvén wave fields (waves parallel and antiparallel to $\mathbf{B}$), which are combined to give the Alfvén wave energy density ϵ. ϵ is related to the space-time average of the fluctuating component of the magnetic field δB by $\epsilon = \langle \delta B^2 \rangle / 4\pi$. The dissipation term D expresses the nonlinear dissipation of Alfvén waves in interplanetary space and will be modeled phenomenologically (*Hollweg*, 1978). The term $\mathbf{v} \cdot \nabla p_w$ in eq. (9) is the work done on the Alfvén waves by the plasma flow.

The increased complexity of the improved model makes a step-by-step approach essential. We first incorporated our improved model in a 1-D code, and reproduced the results of *Withbroe* (1988). We have since implemented the model in two dimensions, and performed a preliminary comparison between a polytropic model, a thermodynamic model (heating, parallel thermal conduction, and presence of a transition region), and a thermodynamic model with Alfvén waves. Figure 8 shows this comparison. With the improved thermodynamic model, the observed white light contrast between coronal holes and streamers is reproduced (*Bagenal et al.* 1996), and the wind achieves faster velocities. With Alfvén waves, a larger contrast between the fast and slow wind develops.

The improved model significantly advances our capabilities to study the large-scale corona and inner heliosphere. The trade-off is that some of the important physical processes are poorly understood (coronal heating, Alfvén wave dissipation, and collisionless thermal conduction) and must be parameterized. In the results shown in Figure 8, the coronal heating was parameterized as

$$H_{ch} = H_0(\theta)\exp\left[-(r - R_s)/\lambda(\theta)\right] \tag{10}$$

where $H_0(\theta)$ expresses the latitudinal variation of the volumetric heating, and $\lambda(\theta)$ expresses the latitudinal variation of the heating function scale length. For the cases shown in Figure 8, H_0, λ, and the flux of Alfvén waves were assumed to be uniform

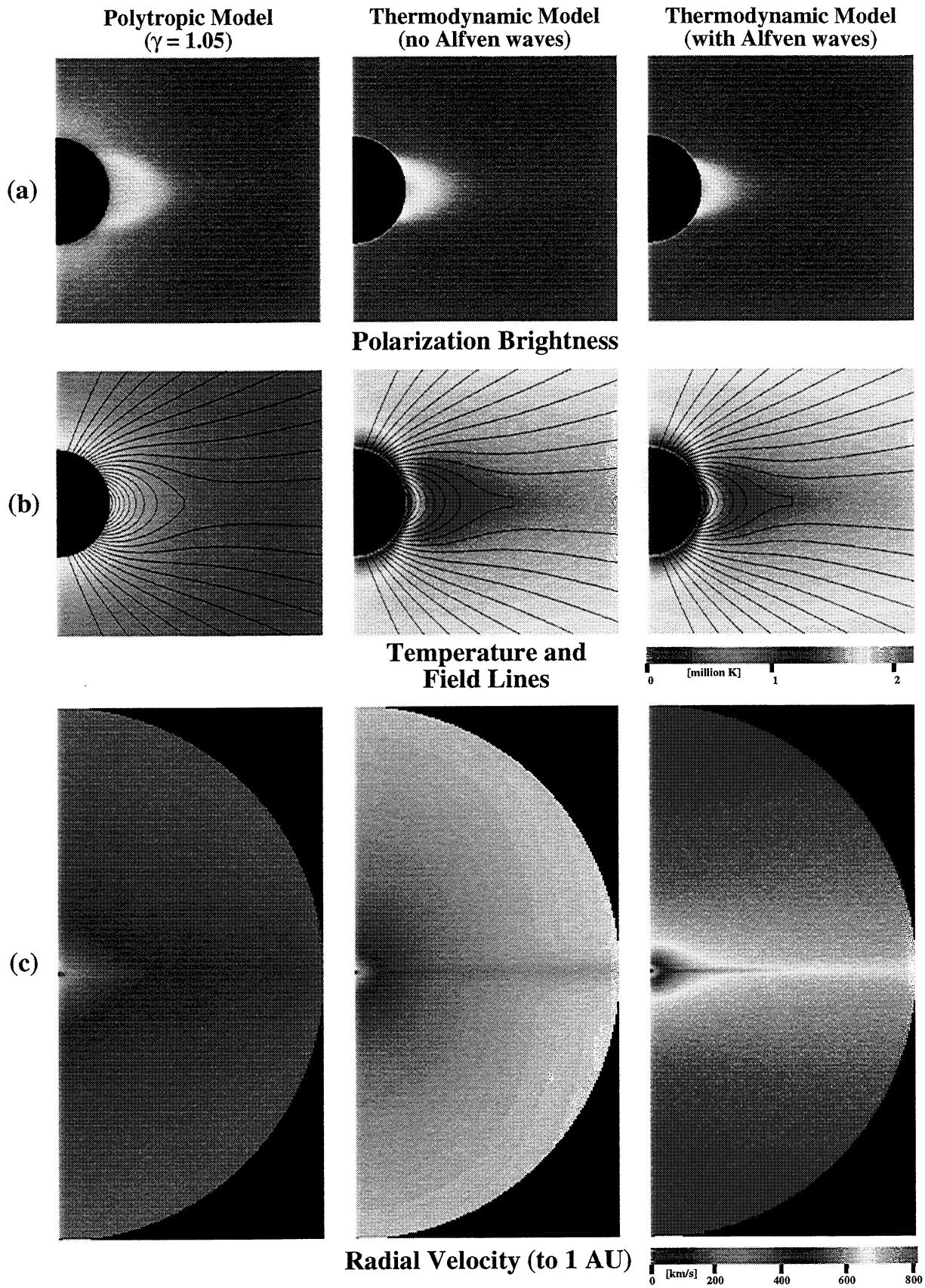

Figure 8. Preliminary comparison between a polytropic model and a thermodynamic model (with and without Alfven waves) for a 2–D simulation with an initial dipole magnetic field. (a) The observed contrast in polarization brightness between coronal holes and streamers is reproduced by the models with improved thermodynamics. (b) With heating and thermal conduction present, the closed field region becomes hotter than the open field. (c) The thermodynamic models predict faster solar wind velocities, especially when Alfven wave acceleration is present. With Alfven waves, a greater contrast between the wind speed at high latitudes and the equator develops.

in latitude. In the future, we plan to study the effects of the different parameters in 2-D, and change the coronal heating to be expressed in terms of magnetic topology (i.e., a proxy for open and closed field regions) rather than latitude θ. Eventually we plan to incorporate the improved thermodynamics into full 3-D solutions, just as we have previously done with the polytropic model.

5. Publications

Crooker, N. U., A. H. McAllister, R. J. Fitzenreiter, J. A. Linker, D. E. Larson, K. W. Ogilvie, R. P. Lepping, A. Szabo, J. T. Steinberg, A. J. Lazarus, Z. Mikić, and R. P. Lin, Sector boundary transformation by an open magnetic cloud, submitted to *J. Geophys. Res.*, 1998.

Linker, J. A., & Mikić, Z., Disruption of a helmet streamer by photospheric shear, *Astrophys. J*, 438, L45, 1995.

Linker, J. A., Z. Mikić & D. D. Schnack, Global coronal modeling and space weather prediction, in *Solar Drivers of Interplanetary and Terrestrial Disturbances*, (K. S. Balasubramaniam, S. L. Keil, & R. N. Smartt, eds.), Astron. Soc. Pac. Conf., *95*, 208, 1996.

Linker, J. A., and Z. Mikić, Extending coronal models to Earth orbit, in *Coronal Mass Ejections*, edited by N. Crooker, J. A. Joselyn, and J. Feynman, *Geophys. Monogr. Ser.*, *99*, 269, 1997.

Linker, J. A., Z. Mikić, D. A. Biesecker, R. J. Forsyth, S. E. Gibson, A. J. Lazarus, A. Lecinski, P. Riley, A. Szabo, and B. J. Thompson, Magnetohydrodynamic modeling of the solar corona during Whole Sun Month, in preparation, 1998.

Mikić, Z., & J. A. Linker, Large scale structure of the solar corona and inner heliosphere, *Solar Wind 8*, AIP Conf. Proceedings 382, 104, 1996.

Mikić, Z., & J. A. Linker, The initiation of coronal mass ejections by magnetic shear, in *Coronal Mass Ejections: Causes and Consequences*, in press, 1997.

Neugebauer, M., R. J. Forsyth, A. B. Galvin, K. L. Harvey, J. T. Hoeksema, A. J. Lazurus, R. P. Lepping, J. A. Linker, Z.Mikić, R. von Steiger, Y. M. Wang, and R. F. Wimmer-Schweingruber, The spatial structure of the solar wind and comparisons with solar data and models, *J. Geophys. Res.*, in press, 1998.

Van Hoven, G., J. A. Linker, and Z. Mikić, The evolution, structure, and dynamics of the magnetized solar corona, *Gather-Scatter*, 11, 6, 1995.

This contract partially or fully supported 9 invited and 15 contributed presentations at scientific meetings from February, 1995 to February, 1998. Some of our results can be viewed on our WEB page: http://iris023.saic.com:8000/corona/modeling.html

6. References

Altschuler, M.D., & G. Newkirk, *Sol. Phys.*, **9**, 131 (1969).

Bagenal, F., J. A. Linker, & Z. Mikić, *EOS Trans AGU*, (abstract), **77**, S218 (1996).

Bagenal, F., & S. Gibson, *J. Geophys. Res.*, **96**, 17663-17674 (1991).

Billings, D. E., *Guide to the Solar Corona*, Academic Press, p. 232, 1966.

Bogdan, T. J., & B. C. Low, *Astrophys. J.*, **306**, 271 (1986).

Endler, F., Ph. D. Thesis, Gottingen Univ. (1971).

Esser, R., & S. R. Habbal, *Geophys. Res. Lett.*, **22**, 22661 (1995).

Feynman, J., & S. F. Martin, *J. Geophys. Res.*, **100**, 3355 (1995).

Gibson, S., & F. Bagenal, *J. Geophys. Res.*, **100**, 19865-19880 (1995).

Gibson, S., F. Bagenal, & B. C. Low, *J. Geophys. Res.*, **101**, 4813-4823 (1996).

Habbal, S. R., R. Esser, M. Guhathakurta, & R. Fisher, *Geophys. Res. Lett.*, **22**, 1465 (1995).

Habbal, S. R., R. Esser, M. Guhathakurta, & R. Fisher, in Solar Wind 8, (D. Winterhalter, J. T. Golsing, S. R. Habbal, W. S. Kurth, & M. Neugebauer eds.) *AIP Conf. Proceedings*, **382**, 129, (1996).

Hoeksema, J. T., Tech. Rep. CSSA-ASTRO-84-07, Center for Space Science and Astronomy, Stanford University, California (1984).

Hoeksema, J. T., Tech. Rep. CSSA-ASTRO-91-01, Center for Space Science and Astronomy, Stanford University, California (1991).

Hoeksema, J. T., & S. T. Suess, *Mem. S.A.It.*, **61**, 485 (1990).

Hollweg, J. V., *Rev. Geophys. Space Phys.*, **16**, 689 (1978).

Jacques, S. A., *Ap. J.*, **215**, 942 (1977).

Linker, J. A., G. Van Hoven, & D. D. Schnack, *Geophys. Res. Lett.*, **17**, 2281 (1990).

Linker, J. A., & Z. Mikić, *EOS Trans. AGU*, **75**, 281 (1994).

Linker, J. A., & Z. Mikić, *Astrophys. J.*, **438**, L-45 (1995).

Linker, J. A., Z. Mikić, & D. D. Schnack, in Solar Drivers of Interplanetary and Terrestrial Disturbances, (K. S. Balasubramaniam, S. L. Keil, & R. N. Smartt, eds.), *Astron. Soc. Pac. Conf.*, **95**, 208 (1996).

Linker, J. A., & Z. Mikić, in Coronal Mass Ejections: Causes and Consequences, in press, 1997.

Mikić, Z., & J. A. Linker, *Astrophys. J.*, **430**, 898 (1994).

Mikić, Z., J. A. Linker, & D. D. Schnack, in Solar Drivers of Interplanetary and Terrestrial Disturbances, *Astron. Soc. Pac. Conf.*, **95**, 108 (1996).

Mikić, Z., & J. A. Linker, *Solar Wind 8*, AIP Conf. Proceedings 382, 104, 1996.

Mikić, Z., & A. N. McClymont, in Solar Active Region Evolution: Comparing Models with Observations (K. S. Balasubramaniam & G. W Simon, eds), *Astron. Soc. Pac. Conf.* **68**, 225 (1994).

Neugebauer, M., R. J. Forsyth, A. B. Galvin, K. L. Harvey, A. J. Lazurus, R. P. Lepping, J. A. Linker, Z. Mikić, R. von Steiger, Y. M. Wang, & R. F. Wimmer, *EOS Trans. AGU*, (abstract), **78**, S258, 1997.

Parker, E. N., *Interplanetary Dynamical Processes*, Interscience publishers, New York (1963).

Parker, E. N., *Spontaneous Current Sheets in Magnetic Fields* (New York: Oxford) (1994).

Pneuman, G. W., & R. A. Kopp, *Solar Phys.*, **18**, 258 (1971).

Rosner, R., W. H. Tucker, & G. S. Vaiana, *Ap. J.*, **220**, 643 (1978).

Schatten, K. H., J. M. Wilcox, & N. Ness, *Solar Phys.*, **6**, 442 (1969).

Schatten, K. H., *Cosmic Electrodyn.*, **2**, 232 (1971).

Schulz, M., *Space Science Rev.*, **72**, 149 (1995).

Smith, E. J., A. Balogh, M. E. Burton, G. Erdos, & R. J. Forsyth, *Geophys. Res. Lett.*, **22**, 3325 (1995).

Steinolfson, R. S., S. T. Suess, & S. T. Wu, *Astrophys. J.*, **255**, 730 (1982).

Stewart, G. A., & S. Bravo, in Solar Wind 8, (D. Winterhalter, J. T. Gosling, S. R. Habbal, W. S. Kurth, & M. Neugebauer eds.) AIP Conf. Proceedings, **382**, 145 (1996).

Suess, S. T., A. H. Wang, & S. T. Wu, *J. Geophys. Res.*, **101**, 19957 (1996).

Usmanov, A. V., in Solar Wind 8, (D. Winterhalter, J. T. Gosling, S. R. Habbal, W. S. Kurth, & M. Neugebauer eds.), *AIP Conf. Proceedings*, **382**, 141 (1996).

Wang, A. H., S. T. Wu, S. T. Suess, & G. Poletto, *Sol. Phys.*, **147**, 55 (1993).

Wang, Y. M., & N. R. Sheeley, *J. Geophys. Res.*, **93**, 11,227 (1988).

Wang, Y. M., & N. R. Sheeley, Jr., *Astrophys. J.*, **392**, 310 (1992).

Washimi, H., Y. Yoshino, & T. Ogino, *Geophys. Res. Lett.*, **14**, 487 (1987).

Withbroe, G. L., *Astrophys. J.*, **325**, 442 (1988).

Zhao, X., & J. T. Hoeksema, *J. Geophys. Res.*, **100**, 19 (1995).